



Activity and stability of NiCe@SiO₂ multi-yolk-shell nanotube catalyst for tri-reforming of methane

Sunkyu Kim^a, Bradie S. Crandall^a, Michael J. Lance^b, Nicole Cordonnier^a, Jochen Lauterbach^a, Erdem Sasmaz^{a,*}

^a Smartstate Center for Strategic Approaches to the Generation of Electricity (SAGE), Department of Chemical Engineering, University of South Carolina, 541 Main Street, Columbia, South Carolina 29208, United States

^b Materials Science and Technology Division, Oak Ridge National Laboratory, Oak Ridge, Tennessee 37831, United States



ARTICLE INFO

Keywords:
 CO₂ utilization
 Nickel
 Syngas
 Tri-reforming of methane
 Yolk-shell

ABSTRACT

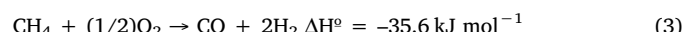
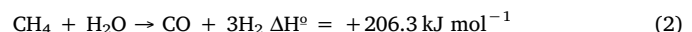
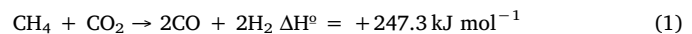
Tri-reforming of methane (TRM) produces syngas by directly utilizing flue gas from a fossil fuel-fired power plant without requiring post-combustion CO₂ separation. In this work, different yolk sizes of a NiCe@SiO₂ multi-yolk-shell nanotube catalyst were prepared and their catalytic properties were evaluated at different oxidizer (CO₂ + H₂O + O₂) to methane (O/M) feed ratios for TRM. The NiCe@SiO₂ multi-yolk-shell nanotube catalyst can exhibit longer stability than the conventional NiCe/SiO₂^{imp} catalyst synthesized by impregnation method due to its controlled morphology and synergistic interactions of Ni–Ce and Ni–Si species. At a low O/M feed ratio of 1.0, NiCe@SiO₂ with smaller yolks (< 20 nm) shows higher resistance to carbon deposition than NiCe@SiO₂ with larger yolks due to the facile oxidation of carbon. On the other hand, NiCe@SiO₂ with larger yolks (> 30 nm) presents stable TRM activity at a high O/M feed ratio of 1.1, whereas NiCe@SiO₂ consisting of smaller yolks deactivates. Deactivation of NiCe@SiO₂ with smaller yolks can be explained by the re-oxidation of active Ni species, in which carbon formation and oxidation rates, and Ce³⁺/Ce⁴⁺ redox properties play a crucial role. Our results indicate that the NiCe@SiO₂ multi-yolk-shell nanotube structures can provide high TRM activity, yet their structure should be tuned for stable performance by considering the yolk sizes and interaction of Ni–Ce species.

1. Introduction

CO₂ is the primary greenhouse gas, accounting for 82% of the United States (US) greenhouse gas emissions from human activities [1]. The combustion of fossil fuels for electricity generation remains the largest source of CO₂ emissions in the US [1–3]. CO₂ emissions are related to energy consumption and economic growth, and need to be controlled to mitigate their effect on climate change [4]. Many concepts have been explored to utilize CO₂ as a feedstock, including hydrogenation, reforming, mineralization, photoreduction, electroreduction, co-polymerization and bio-catalytic conversion [5–8]. Among them, syngas production through the application of reforming is proposed to be a valuable technology, which can be developed in the midterm by using novel catalytic routes to break C–O bonds and convert CO₂ to valuable chemicals [5,9,10].

Tri-reforming of methane (TRM) is a unique process that can be applied to utilize CO₂ emissions directly from a combustion source using natural gas as the primary reactant [11–14]. It has been reported

that fossil fuel-fired power plants integrated with the TRM process could reduce CO₂ emissions by up to 85% [15]. TRM involves synergistic combination of dry reforming of methane (DRM, (1)), steam reforming of methane (SRM, (2)), and partial oxidation of methane (POM, (3)) as shown in the following reactions:



In TRM, the CO₂ in the flue gas can be converted to syngas by DRM. DRM produces a H₂/CO molar ratio of 1, which can potentially be used for the production of liquid hydrocarbons and oxygenates [16]. Although DRM has the advantage of utilizing CO₂ as an oxidizer, it is a highly endothermic reaction, needs a “pure” CO₂ stream and suffers from carbon deposition leading to catalyst deactivation [17–19]. Coupling DRM with SRM and POM can provide the advantage of adjusting the H₂/CO molar ratios between 1 and 2.5, desired for the

* Corresponding author at: Department of Chemical Engineering, University of South Carolina, Columbia, SC 29208, United States.
 E-mail address: sasmaz@cec.sc.edu (E. Sasmaz).

Fischer–Tropsch, methanol, and dimethyl ether synthesis [20–24]. Incorporation of H_2O and O_2 as an oxidizer into the feed stream can eliminate carbon deposition and reduce energy needs through POM [25,26]. The synergistic combination of three reactions in TRM eliminates the need to pre-separate CO_2 , which can further decrease the energy consumption and cost of operation.

Nickel-based catalysts are widely studied for TRM as they have a low cost compared to noble metals and have high activity at 750 °C [11,12,14,27,28]. Nickel structures supported or promoted with CeO_2 can improve the TRM activity, as CeO_2 can store and release oxygen reversibly due to its oxygen vacancies and reversible valence redox property ($\text{Ce}^{3+}/\text{Ce}^{4+}$) [29,30]. The addition of promoters to the Ni-based catalysts can further increase the activity and stability of the material by strengthening the metal–support interaction, providing high oxygen storage capacity and creating strong basic sites for CO_2 activation [31–33]. In addition to the promoters, the effect of CeO_2 -based supports on TRM activity has been investigated, in which small Ni particle sizes on CeO_2 -based supports are reported to be beneficial for stable activity [34,35]. In these earlier studies, the effect of promoters or order of metal impregnation on the TRM activity has been examined. However, the interaction among active Ni, promoter, and support, and the effect of particle size on the TRM activity has not been identified.

Catalyst morphologies with unique physical and chemical properties, i.e., core/yolk–shell structures, have been investigated in reforming reactions and shown to have high resistance to carbon deposition and sintering due to the confinement effect and enhanced metal support interaction [36–45]. Compared to the core–shell, the yolk–shell structures (Scheme 1) can have a void space between the core metals and the outer shell materials that can provide additional properties to the material. The unique nanoreactor environment of the yolk–shell can facilitate chemical storage and confinement of the reactants, intermediates, and products. The cavity between the yolk and shell provides not only high exposed active areas but also a homogenous environment for catalysis [46–50]. Few papers have been published on the core/yolk–shell catalysts for DRM and POM. These studies emphasize that shell thickness, yolk size, pore size and porosity can influence the activity and stability of core/yolk–shell catalysts for DRM [51–53]. In addition, core–shell catalysts promoted with La and Ce can further improve the stability of the catalyst by reducing the surface carbon growth in DRM and POM [46,54]. To date, there is only one study reported the activity of a $\text{Ni}@\text{SiO}_2$ core–shell catalyst under various feed stream concentrations of TRM. In this study, formation of a core–shell structure is inconclusive and the effect of Ni particle size on the TRM activity at various oxidizer to methane feed ratios could not be understood [55].

It is important to note that TRM can be operated at different oxidizer ($\text{CO}_2 + \text{H}_2\text{O} + \text{O}_2$) to methane (O/M) feed ratios. Variations in methane concentration in the feed stream can dramatically influence

the catalyst performance for TRM. Generally, a catalyst for TRM should be able to exhibit high carbon resistance under reducing conditions ($\text{O}/\text{M} \leq 1$), while re-oxidation of active metallic Ni to Ni^{2+} should be hindered under oxidizing conditions ($\text{O}/\text{M} > 1$) [55,56]. Most of the studies involving core/yolk–shell structures were performed under DRM conditions. The effects of catalyst morphology and Ni–promoter interaction on the TRM activity at various O/M feed ratios have not been investigated. In this work, we have evaluated the TRM activity and stability of $\text{NiCe}@\text{SiO}_2$ multi–yolk–shell nanotube catalysts at different O/M feed ratios, and identified the influence of yolk size and Ni–Ce interaction on the catalytic performance. To the best of our knowledge, this is the first study reporting the effect of morphology on the activity of the yolk–shell structured catalysts at various O/M feed ratios under TRM.

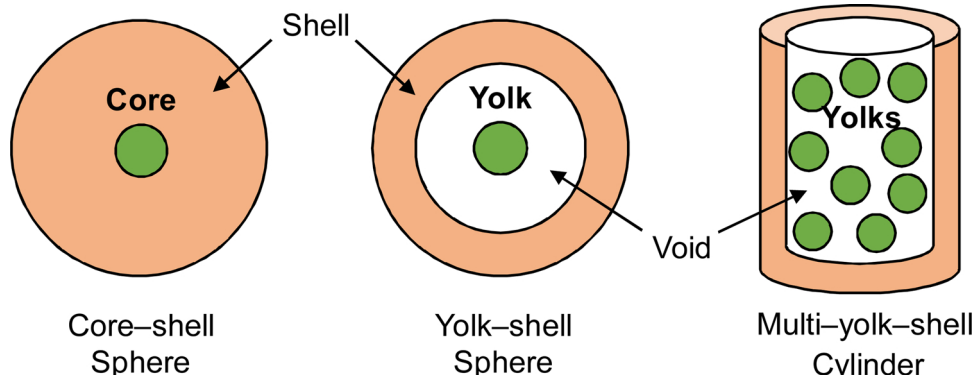
2. Experimental methods

2.1. Materials

The chemical reagents were used as purchased without any further purification: Nickel nitrate hexahydrate ($\text{Ni}(\text{NO}_3)_2 \cdot 6\text{H}_2\text{O}$, 98%, Alfa Aesar) and cerium nitrate hexahydrate ($\text{Ce}(\text{NO}_3)_3 \cdot 6\text{H}_2\text{O}$, 99%, Sigma Aldrich) were used as the Ni and Ce yolk precursors. 1-hexadecyl trimethyl ammonium bromide (CTAB) ($\text{CH}_3(\text{CH}_2)_{15}\text{N}(\text{CH}_3)_3\text{Br}$, 98%, Alfa Aesar) was used as the surfactant and 1-butanol ($\text{CH}_3(\text{CH}_2)_3\text{OH}$, anhydrous, 99.8%, Sigma Aldrich) and cyclohexane (C_6H_{12} , 99%, Alfa Aesar) were used as the oil phase in the microemulsion solution. Hydrazine (N_2H_4 , anhydrous, 98%, Sigma Aldrich) was used as a reducing agent and tetraethyl orthosilicate (TEOS) ($\text{Si}(\text{OC}_2\text{H}_5)_4$, 99% Sigma Aldrich) was used as the silica shell precursor. Sodium hydroxide (NaOH , Fisher Chemical) and ammonium hydroxide solution (NH_4OH , 28% NH_3 , Alfa Aesar) were used for base environmental conditions during the synthesis. Fumed silica (SiO_2 , Sigma Aldrich) and Ethanol ($\text{C}_2\text{H}_6\text{O}$, anhydrous, Fisher Chemical) were used for synthesizing wet impregnated catalyst, and deionized (DI) water was used throughout the procedure. Methane (3.7 UHP, Praxair), CO_2 (4.8 research, Praxair), air (ultra zero, Praxair), and N_2 (100%, Airgas) were used for the tri-reforming of methane reaction.

2.2. Catalyst synthesis

The $\text{NiCe}@\text{SiO}_2$ multi–yolk–shell nanotube catalyst was synthesized by reverse microemulsion method. The solution containing 0.2 M $\text{Ni}(\text{NO}_3)_2 \cdot 6\text{H}_2\text{O}$ and 0.05 M $\text{Ce}(\text{NO}_3)_3 \cdot 6\text{H}_2\text{O}$ in 4 ml of DI water was added dropwise to the microemulsion dissolved in 0.17–0.26 M CTAB in 15 ml of 1-butanol and 80 ml of cyclohexane mixture. After stirring the solution for 1 h, the transparent microemulsion solution was heated up to 70 °C in an oil bath, and 0.7 ml of hydrazine with 0.5 M NaOH in 1.5 ml DI was added to the solution dropwise, followed by further stirring for



Scheme 1. Schematic illustration of the core–shell, yolk–shell, and multi–yolk–shell nanotube structures.

40 min. The solution was cooled down to room temperature, and aged for another 2 h under stirring. Finally, 1.5 ml of TEOS was added to the solution dropwise, and after 1 h, 1.5 ml of ammonium hydroxide solution was added to the solution dropwise. The final solution was aged for 1 day for hydrolysis and condensation of the silica precursor. The solution was washed with ethanol and separated by centrifuging. The washed sample was dried at 100 °C overnight, and then calcined in static air at 500 °C for 4 h with a ramping rate of 5 °C min⁻¹. Different yolk sizes and tube diameters can be obtained by controlling the water to surfactant (CTAB) molar ratio. A low water/CTAB ratio leads to larger yolk size with a shorter tube diameter, and a high water/CTAB ratio forms a smaller yolk size with a longer tube diameter. NiCe@SiO₂^A, NiCe@SiO₂^B, and NiCe@SiO₂^C catalysts were prepared in a water to CTAB ratio of 12.6, 15.8, and 18.9, respectively. For comparison, conventional NiCe/SiO₂^{Imp} was synthesized by a wet impregnation method. 0.02 M Ni(NO₃)₂·6H₂O, 0.005 M Ce(NO₃)₃·6H₂O, and 0.5 g of silica were mixed in 50 ml ethanol. The whole mixture was stirred overnight, and the material was dried at 100 °C overnight, followed by calcination at 500 °C in stagnant air for 4 h with ramping temperature rate of 5 °C min⁻¹.

2.3. Catalyst activity measurements

The performance of the catalyst for TRM was tested in a fixed-bed reactor at atmospheric pressure. 75 mg of the catalyst was placed between quartz wool in a quartz reactor with an inner diameter of 7 mm. Water was injected into an evaporator via a peristaltic pump and mixed with the reaction gases. The reaction gases (CH₄, CO₂, O₂, and N₂) were introduced to the evaporator via mass flow controllers. The reactor was placed in a furnace and the temperature of the catalyst was measured by a K-type thermocouple placed inside the catalyst bed. The effluent gases were passed through a condenser in which water vapor was removed, and their concentration was measured with a gas chromatograph (GC) using a thermal conductivity detector (TCD). Prior to the reaction, all catalysts were reduced at 600 °C for 1 h with 25% H₂ balanced with N₂. Following the reduction, the catalysts were heated up to a reaction temperature of 750 °C under N₂ flow. The TRM reaction was carried out for 20 h in a gas hourly space velocity (GHSV) of 60,000 ml g⁻¹ h⁻¹ at different O/M feed ratios including 0.85 (CH₄ : CO₂ : H₂O : O₂ = 2.59 : 1 : 1 : 0.2), 1 (CH₄ : CO₂ : H₂O : O₂ = 2.2 : 1 : 1 : 0.2), 1.1 (CH₄ : CO₂ : H₂O : O₂ = 2 : 1 : 1 : 0.2) and 1.25 (CH₄ : CO₂ : H₂O : O₂ = 1.76 : 1 : 1 : 0.2). The catalytic activity was calculated using the following equations:

$$\text{Conversion (\%)} = \frac{F_{\text{react,in}} - F_{\text{react,out}}}{F_{\text{react,in}}} \times 100 \quad (4)$$

$$\text{H}_2 \text{ yield (\%)} = \frac{F_{\text{H}_2,\text{out}}}{2F_{\text{CH}_4,\text{in}} + F_{\text{H}_2\text{O,in}}} \times 100 \quad (5)$$

$$\text{CO yield (\%)} = \frac{F_{\text{CO},\text{out}}}{F_{\text{CO}_2,\text{in}} + F_{\text{CH}_4,\text{in}}} \times 100 \quad (6)$$

$$\text{H}_2/\text{CO r atio} = \frac{F_{\text{H}_2,\text{out}}}{F_{\text{CO},\text{out}}} \quad (7)$$

where F is the molar flow rate of the reagent species measured at the inlet and outlet of the reactor. The reproducibility of the catalytic activity for all experiments is within ± 5%.

2.4. Characterization

Field emission scanning electron microscopy (FESEM, Zeiss Ultra plus) and transmission electron microscopy (TEM, Hitachi H8000) images were obtained to investigate the morphology of the catalysts. Histogram distributions of yolk size was generated by analyzing TEM images, and 100 yolks were used for each distribution. The elemental

mapping of the catalysts was collected using a scanning transmission electron microscope (STEM, FEI Talos F200X). The weight percent of Ni and Ce in the samples was analyzed by inductively coupled plasma atomic emission spectroscopy (ICP-OES, Optima 2000 DV). Powder X-ray diffraction (XRD) patterns of the catalysts were obtained by using a Rigaku MiniFlex II with CuK_α source radiation ($\lambda = 1.5406$) for 20 range of 10°–80° with a step rate of 2° min⁻¹. The crystallite size of the components was calculated using Scherrer equation from the peaks at the (111) phase of each chemical element. The specific surface area of the sample was measured using a Micromeritics ASAP 2020. The samples were degassed at 300 °C for 7 h to remove the moisture prior to the measurements. Hydrogen temperature programmed reduction (H₂-TPR) was performed using a Micromeritics AutoChem II to identify the interaction between active species and supports and determine the reducibility of the catalysts. First, 50 mg of catalyst was heated up to 300 °C and held for 1 h under He flow to eliminate moisture and contaminations, and then cooled down to 30 °C. After the preparation step, the temperature of the catalyst was increased from 30 °C to 900 °C at a ramping rate of 10 °C min⁻¹ in a 10% H₂/Ar mixture, and the H₂ consumption was monitored by TCD. The amount of H₂ reduced was calibrated by using CuO. H₂ pulse chemisorption experiments were performed with the same apparatus as H₂-TPR to determine the dispersion of Ni particles. First, 100 mg of catalyst was reduced under 10% H₂/Ar at 600 °C for 5 h. Then the catalyst was purged at 610 °C for 1 h and cooled down to 35 °C under He flow. H₂ pulse chemisorption was conducted at 35 °C in 10% H₂/Ar with 8 min intervals. The oxidation states of the elements presented in catalysts were determined by X-ray photoelectron spectroscopy (XPS) with a Kratos Axis Ultra DLD using AlK_α radiation, and the binding energy was calibrated to the signal of C 1s at 284.8 eV. The spectra were obtained after the samples were reduced in H₂AlK₂ at 600 °C for 1 h. Thermogravimetric analysis (TGA) was employed using a TGA-50 Shimadzu to determine carbon deposition on the spent catalyst. The sample weight loss was characterized under air flow from 30 °C to 900 °C with a ramping temperature of 10 °C min⁻¹. Raman spectra were obtained using an XploRA PLUS system from Horiba in the backscattering configuration at a 638 nm wavelength to determine the nature of carbon formed on the spent catalyst.

3. Results and discussion

3.1. Characterization of the fresh catalysts

Fig. 1 (a)–(c) show TEM images of NiCe@SiO₂^A, NiCe@SiO₂^B, and NiCe@SiO₂^C multi-yolk-shell nanotube catalysts synthesized in a solution containing water/CTAB molar ratios of 12.6, 15.8, and 18.9, respectively. The yolk nanoparticles of each catalyst are shown to be dispersed uniformly with a mean size of 32.9 nm, 23.7 nm, and 20.0 nm for NiCe@SiO₂^A, NiCe@SiO₂^B, and NiCe@SiO₂^C, respectively. The yolks of NiCe@SiO₂^A, NiCe@SiO₂^B, and NiCe@SiO₂^C are encapsulated by SiO₂ with an average tube diameter of 41.8 nm, 243.0 nm, and 275.0 nm, respectively. The multi-yolk-shell nanotube structure prepared at a high concentration of CTAB, i.e. NiCe@SiO₂^A, consists of larger yolks with a smaller diameter tube, whereas the multi-yolk-shell nanotube structure synthesized at a low concentration of CTAB, i.e. NiCe@SiO₂^C, has smaller yolks within a larger diameter tube. Compared to the multi-yolk-shell nanotube structured catalysts, conventional NiCe/SiO₂^{Imp} synthesized by a wet impregnation method does not show any specific morphology (**Fig. 1** (d)). It is important to note that Ce species are necessary to generate nanotube morphology. For instance, it is observed that Ni@SiO₂ without Ce forms a spherical yolk-shell structure rather than a nanotube structure when similar amount of Ni existed as in NiCe@SiO₂ (**Fig. S1**). This is because the nanotube formation and elongation is limited by the amount of gas released during the synthesis, in which Ce ions produce double amount of N₂ in comparison to Ni ions during reduction with hydrazine [57].

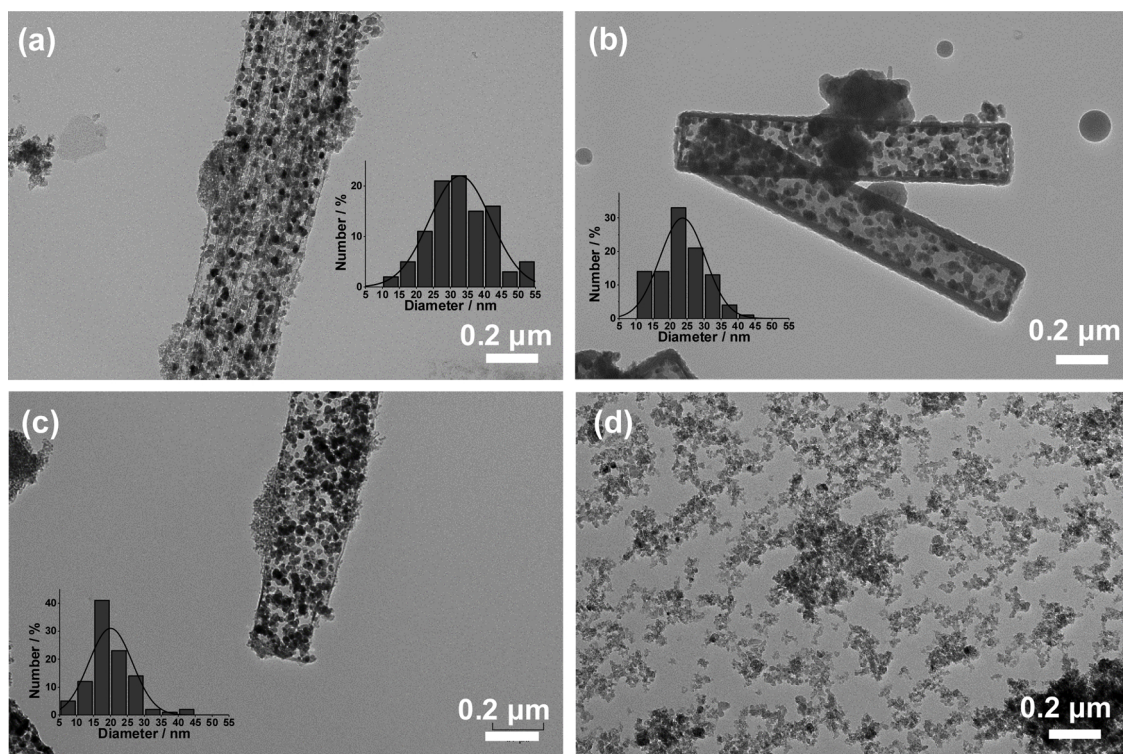


Fig. 1. TEM images of as-synthesized multi-yolk-shell nanotube catalysts synthesized in different water to CTAB ratios of (a) 12.6 ($\text{NiCe}@\text{SiO}_2^{\text{A}}$), (b) 15.8 ($\text{NiCe}@\text{SiO}_2^{\text{B}}$), (c) 18.9 ($\text{NiCe}@\text{SiO}_2^{\text{C}}$) solution. The inset graph shows yolk size distribution. (d) TEM image of $\text{NiCe}/\text{SiO}_2^{\text{Imp}}$ synthesized by wet impregnation.

As shown in **Fig. 2**, the elemental mapping of STEM images of the $\text{NiCe}@\text{SiO}_2^{\text{A}}$ and $\text{NiCe}@\text{SiO}_2^{\text{C}}$ catalysts confirm that the yolks are composed of Ni species surrounded by an outer shell consisting of only SiO_2 . As shown in **Fig. 2 (a)**, accumulation of Ce on larger Ni yolks in $\text{NiCe}@\text{SiO}_2^{\text{A}}$ can be more pronounced than that in $\text{NiCe}@\text{SiO}_2^{\text{C}}$ with smaller yolks. Ce is found to be more dispersed throughout the catalysts, yet it is mostly accumulated on the Ni yolks indicating the possible Ni-Ce interaction. It is important to note that characteristic X-ray signals detected for Ce in the energy dispersive X-ray (EDX) spectra is low compared to Ni and Si. Although most of the Ce components are inside the nanotube structures, Ce pixels observed outside the nanotubes are possibly due to the low signal-to-noise ratio. The contrast change of Si between the edges and inner parts of the nanotube indicates that the SiO_2 shell has a cylindrical tube morphology with the presence of interstitial voids. Both the TEM and STEM images cannot definitively confirm whether the nanotubes are capped at each end. However, the overview SEM images of $\text{NiCe}@\text{SiO}_2^{\text{C}}$, shown in **Fig. S2**, confirm that the tube structure is hollow in the inside, and both Ni and Ce particles are attached to the inner walls of the hollow tube.

The XRD measurements of the as-synthesized $\text{NiCe}@\text{SiO}_2^{\text{A}}$, $\text{NiCe}@\text{SiO}_2^{\text{C}}$, and $\text{NiCe}/\text{SiO}_2^{\text{Imp}}$ are shown in **Fig. 3**. All three catalysts show NiO and CeO_2 diffraction patterns with an amorphous SiO_2 structure. The peaks at 2-theta of 37.66° , 43.69° , and 63.24° are identified as NiO , and the other peaks at 29.20° , 33.74° , 48.10° , 56.92° , and 75.74° belong to the cubic CeO_2 structure. The broad peak at 21.26° indicates the formation of amorphous SiO_2 shell. Based on the XRD patterns, the $\text{NiCe}@\text{SiO}_2^{\text{A}}$ catalyst shows the largest NiO crystallite size of 18.3 nm , followed by 16.2 nm for $\text{NiCe}@\text{SiO}_2^{\text{C}}$ and 14.3 nm for $\text{NiCe}/\text{SiO}_2^{\text{Imp}}$ (**Table 1**). The crystallite sizes of CeO_2 for the $\text{NiCe}@\text{SiO}_2^{\text{A}}$, $\text{NiCe}@\text{SiO}_2^{\text{C}}$ and $\text{NiCe}/\text{SiO}_2^{\text{Imp}}$ catalysts are found to be 6.7 nm , 8.5 nm , and 4.3 nm , respectively. $\text{NiCe}/\text{SiO}_2^{\text{Imp}}$ has the lowest CeO_2 crystallite size suggesting that ceria has higher dispersion and larger amount of oxygen vacancies than $\text{NiCe}@\text{SiO}_2^{\text{A}}$ followed by $\text{NiCe}@\text{SiO}_2^{\text{C}}$ [58]. The average yolk size of $\text{NiCe}@\text{SiO}_2^{\text{A}}$ measured by TEM (32.9 nm) is much larger than the NiO crystallite size calculated by XRD (18.3 nm) indicating

that the yolks in $\text{NiCe}@\text{SiO}_2^{\text{A}}$ are possibly formed with grain. On the other hand, the average yolk size of $\text{NiCe}@\text{SiO}_2^{\text{C}}$ by TEM (20.0 nm) matches reasonably well with the NiO crystallite size (16.2 nm). **Fig. S3** represents the XRD patterns of $\text{NiCe}@\text{SiO}_2^{\text{A}}$, $\text{NiCe}@\text{SiO}_2^{\text{C}}$, and $\text{NiCe}/\text{SiO}_2^{\text{Imp}}$ after one hour of H_2 reduction at 600°C . The peaks at 2-theta of 45.08° , 52.4° , and 76.84° correspond to metallic Ni phase. The NiO phase is not detected, which indicates that NiO was fully reduced to metallic Ni in all catalysts. The Ni crystallite size of $\text{NiCe}/\text{SiO}_2^{\text{Imp}}$ has the smallest value of 10.4 nm followed by 12.2 nm for $\text{NiCe}@\text{SiO}_2^{\text{A}}$ and 14.9 nm for $\text{NiCe}@\text{SiO}_2^{\text{C}}$. The crystalline CeO_2 peaks get broader after the reduction, indicating that the phase transition of crystalline CeO_2 into Ce_2O_3 has been initiated. For $\text{NiCe}/\text{SiO}_2^{\text{Imp}}$, no CeO_2 peaks are observed due to the formation of highly dispersed CeO_x particles [59].

The textural properties of the catalysts such as specific surface area and metal weight percentages are presented in **Table 1**. The $\text{NiCe}@\text{SiO}_2^{\text{A}}$ catalyst with smaller tube diameter provides larger surface area than the $\text{NiCe}@\text{SiO}_2^{\text{C}}$ catalyst, while the $\text{NiCe}/\text{SiO}_2^{\text{Imp}}$ catalyst has the highest surface area of $486.0\text{ m}^2\text{ g}^{-1}$ among three catalysts. The weight percentages of Ni and Ce are measured to be in between $7.2\text{--}8.2\text{ wt.\%}$ and $4.6\text{--}5.3\text{ wt.\%}$ by ICP-OES in all three catalysts, respectively. The nitrogen adsorption-desorption isotherms of the $\text{NiCe}@\text{SiO}_2^{\text{A}}$, $\text{NiCe}@\text{SiO}_2^{\text{C}}$, and $\text{NiCe}/\text{SiO}_2^{\text{Imp}}$ catalysts are shown in **Fig. S4**. The isotherms of $\text{NiCe}@\text{SiO}_2^{\text{A}}$ and $\text{NiCe}@\text{SiO}_2^{\text{C}}$ indicate type IV isotherm with H3 hysteresis, while $\text{NiCe}/\text{SiO}_2^{\text{Imp}}$ has a type IV isotherm with H2 hysteresis. Both H2 and H3 hysteresis indicate that all three catalysts have a porous structure. However, isotherms of type IV with H3 hysteresis can be found in a hierarchical porous structure consisting of mesopores and macropores, which is consistent with the morphology of the multi-yolk-shell nanotube structure [60].

H_2 -TPR experiments were conducted to determine the reducibility of the as-synthesized catalysts and interaction between the active sites and support. The H_2 -TPR profiles of the Ni/SiO_2 , $\text{Ni}/\text{SiO}_2^{\text{Imp}}$, and $\text{Ce}/\text{SiO}_2^{\text{Imp}}$ catalysts were also analyzed to elucidate the effect of the Ce promoter (**Fig. S5**). As shown in **Fig. 4**, three temperature regions are found to exist for the $\text{NiCe}@\text{SiO}_2^{\text{A}}$, $\text{NiCe}@\text{SiO}_2^{\text{C}}$, and $\text{NiCe}/\text{SiO}_2^{\text{Imp}}$

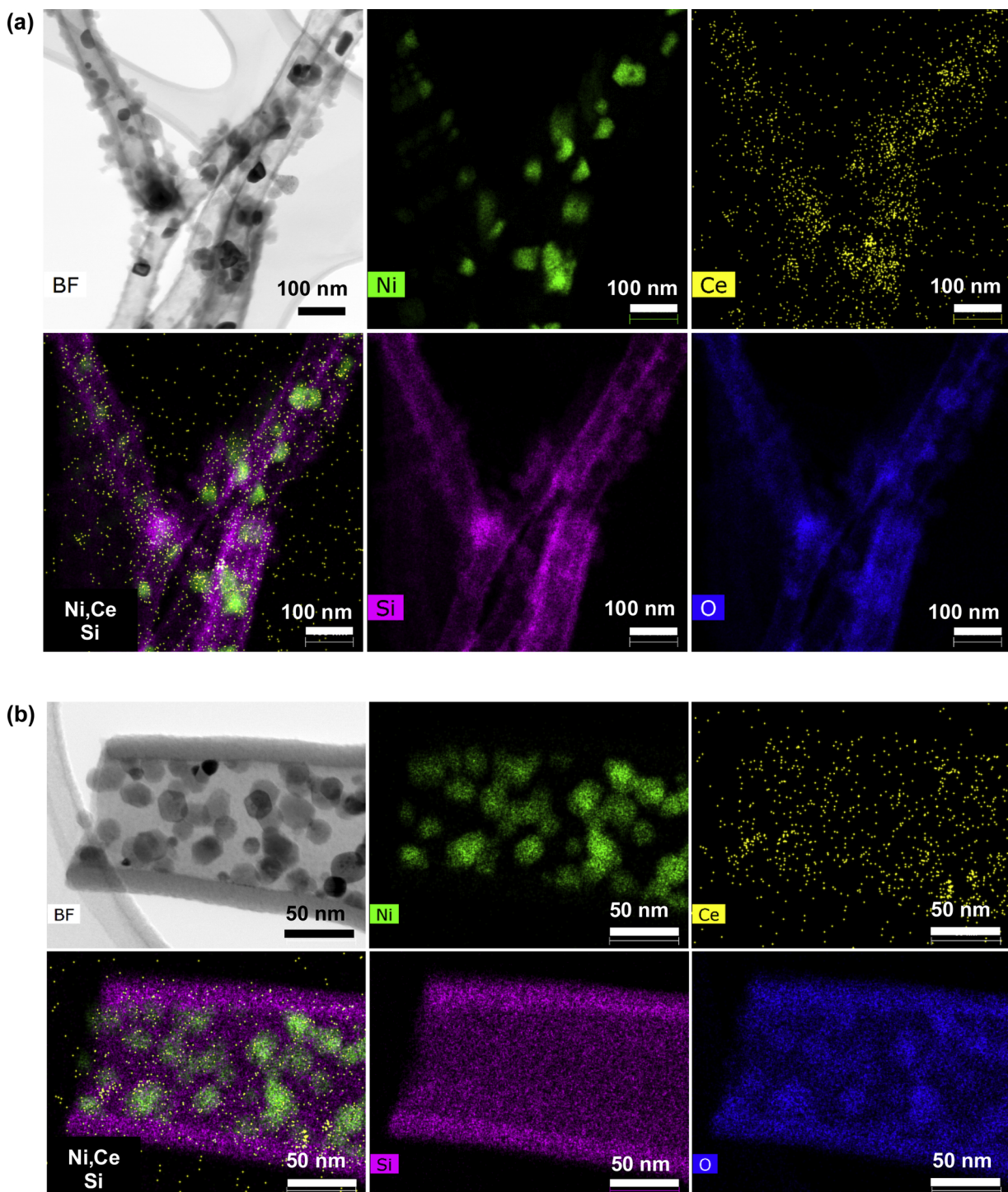


Fig. 2. STEM-EDX elemental mapping (Ni: green, Ce: yellow, Si: magenta, and O: blue) of (a) NiCe@SiO₂^A and (b) NiCe@SiO₂^C (For interpretation of the references to colour in this figure legend, the reader is referred to the web version of this article).

catalysts. The first H₂ consumption peak of α at temperatures between 215 °C and 400 °C is attributed to the combination of two reduction peaks of bulk NiO and aggregated NiO particles interacting more with the oxygen vacancies of CeO₂, in which the latter is expected to be at lower temperatures as oxygen vacancies improve the reducibility of NiO [32,43,61]. Compared to Ni@SiO₂ (Fig. S5), the α peak in the Ce promoted catalysts shifts to a lower temperature (311 °C) for NiCe@SiO₂^A and a higher temperature (333 °C) for NiCe@SiO₂^C. This can be explained by the yolk size effect and the formation of oxygen vacancies in the CeO₂ lattice, as smaller yolks have less Ni-Ce interaction and are

harder to be reduced than the catalyst with larger yolks [62]. The H₂ consumption peak of β in the medium temperature region is associated with the dispersed Ni species interacting with CeO₂ [63]. Formation of the β peak at slightly higher temperatures than the bulk NiO one has been observed by several other researchers [32,62]. It is possible that dispersed Ni particles might have stronger interaction with SiO₂ support, which can shift the Ni-Ce reduction peaks to a higher temperature than the bulk NiO one [46,62]. In the case of NiCe/SiO₂^{Imp}, the α peak consists of NiO particles interacting more with the surface oxygen vacancies of CeO₂, and the NiO reduction peak observed at 352 °C on Ni/

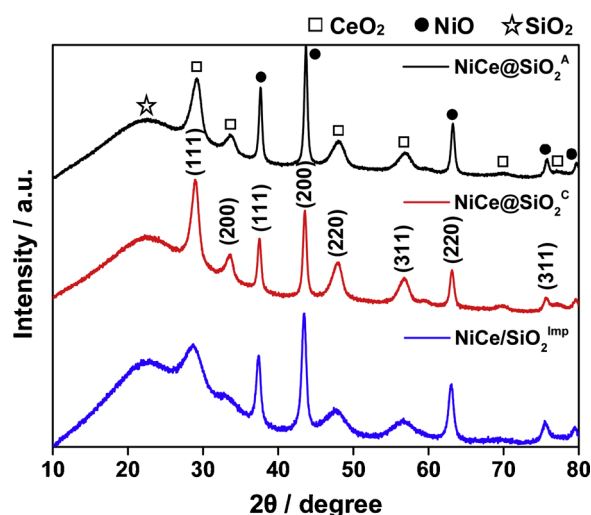


Fig. 3. XRD patterns of as-synthesized NiCe@SiO₂^A, NiCe@SiO₂^C, and NiCe/SiO₂^{Imp}.

SiO₂^{Imp} (Fig. S5) shifts to 386 °C after Ce promotion due to an enhanced NiO–SiO₂ interaction. The H₂ consumption peak of γ at temperatures above 400 °C is assigned to the NiO particles strongly bonded to the SiO₂ support. The broad γ peak for multi-yolk-shell nanotube catalysts is located in a higher temperature region compared to the impregnated catalyst. This indicates that NiO–SiO₂ interaction in NiCe@SiO₂ is stronger than that in NiCe/SiO₂^{Imp} due to the encapsulation of Ni and Ce yolks by mesoporous SiO₂ [38,64]. The H₂ uptake of the multi-yolk-shell nanotube and impregnated catalysts are compared with the actual Ni amount loaded on the catalyst, as shown in Table 2. The overall H₂ consumption is much larger than the theoretical amount of Ni on all three catalysts due to the lattice oxygen reduction of CeO₂ by hydrogen spillover on Ni [32,63]. The H₂ uptake ratio of α/β for the NiCe@SiO₂ multi-yolk-shell nanotube catalyst is approximately 20 times higher than that of NiCe/SiO₂^{Imp} indicating that most of H₂ is consumed by the bulk NiO and aggregated NiO particles interacting with CeO₂. Compared to NiCe@SiO₂^C, the higher overall H₂ consumption observed on NiCe@SiO₂^A indicates that larger yolks are easily reduced due to the formation of more oxygen vacancies in the CeO₂ lattice.

The Ni particle size and dispersion estimated from the H₂ chemisorption measurements is presented in Table 3. For NiCe@SiO₂ multi-yolk-shell nanotube catalysts, Ni particle size is over 290 nm and much larger than the Ni size observed in TEM and XRD. The large particle size obtained for all catalysts from H₂ chemisorption does not represent the actual Ni particle size, indicating that Ni sites are not available to react with H₂. This difference can be explained by the lack of Ni sites for H₂ chemisorption due to the strong Ni–Ce interaction and partially embedded Ni particles in the SiO₂ support [49,50,53]. The effect of latter on Ni particle size has more pronounced in the multi-yolk-shell catalysts compared to the impregnated catalyst, leading to a much larger Ni particle size. As shown in the H₂-TPR experiments (Fig. 4), the γ reduction peak is located at a high temperature for the multi-yolk-shell nanotube catalysts indicating a strong NiO–SiO₂

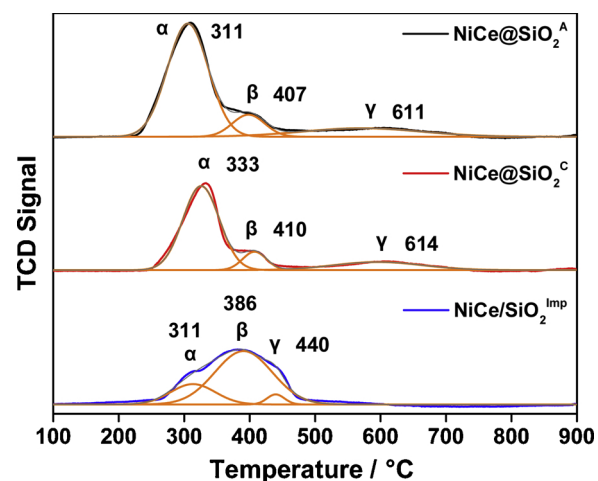


Fig. 4. H₂-TPR profiles of NiCe@SiO₂^A, NiCe@SiO₂^C, and NiCe/SiO₂^{Imp}.

Table 2

H₂ uptake during H₂-TPR experiments with NiCe@SiO₂^A, NiCe@SiO₂^C, and NiCe/SiO₂^{Imp}.

Catalysts	Overall Ni/mmol	H ₂ uptake/mmol			α/β
		α	β	γ	
NiCe@SiO ₂ ^A	0.070	0.084	0.013	0.019	6.5
NiCe@SiO ₂ ^C	0.064	0.056	0.008	0.013	7.0
NiCe/SiO ₂ ^{Imp}	0.053	0.017	0.055	0.003	0.3

Table 3

Physicochemical properties of NiCe@SiO₂^A, NiCe@SiO₂^C, and NiCe/SiO₂^{Imp}.

Catalysts	Ni particle size ^a /nm	Ni dispersion ^a %	Ce ³⁺ /(Ce ³⁺ + Ce ⁴⁺) ^b %
NiCe@SiO ₂ ^A	327.3	0.31	61.6
NiCe@SiO ₂ ^C	292.4	0.35	36.1
NiCe/SiO ₂ ^{Imp}	59.1	1.71	62.9

^a Calculated based on H₂ chemisorption.

^b Obtained from XPS deconvolution.

interaction. Ni dispersion has also been calculated through H₂ chemisorption measurements. As shown in Table 3, The NiCe/SiO₂^{Imp} exhibits the highest Ni dispersion of 1.71%, followed by 0.35% and 0.31% for NiCe@SiO₂^C and NiCe@SiO₂^A, respectively. Ni dispersions have previously been reported in the range of 0.12–0.27% for Ni based core/yolk-shell structures, which are in consistent with our work [53,65]. The higher Ni dispersion observed on NiCe/SiO₂^{Imp} compared to the multi-yolk-shell nanotube catalysts is consistent with the smaller Ni particle size and higher surface area measured on the NiCe/SiO₂^{Imp} catalyst. It is important to note that Ni dispersion on the core/yolk-shell structure in which the active metal is encapsulated by a support can be influenced by the shell material and strong metal–support interaction [53].

Analysis of the core level XPS spectra of Ni and Ce species shows consistent results with the H₂-TPR measurement. As shown in Fig. 5 (a),

Table 1

Textural properties of NiCe@SiO₂^A, NiCe@SiO₂^C, and NiCe/SiO₂^{Imp}.

Catalysts	NiO crystallite size ^a /nm	CeO ₂ crystallite size ^a /nm	S _{BET} /m ² g ⁻¹	Ni loading/wt.%	Ce loading/wt.%
NiCe@SiO ₂ ^A	18.3 ± 0.2	6.7 ± 1.3	400.3	8.2	5.2
NiCe@SiO ₂ ^C	16.2 ± 0.8	8.5 ± 1.1	366.9	7.5	5.3
NiCe/SiO ₂ ^{Imp}	14.3 ± 0.5	4.3 ± 0.3	486.0	7.2	4.6

^a Crystallite size of NiO and CeO₂, estimated according to the Scherrer equation applied to (111) phase.

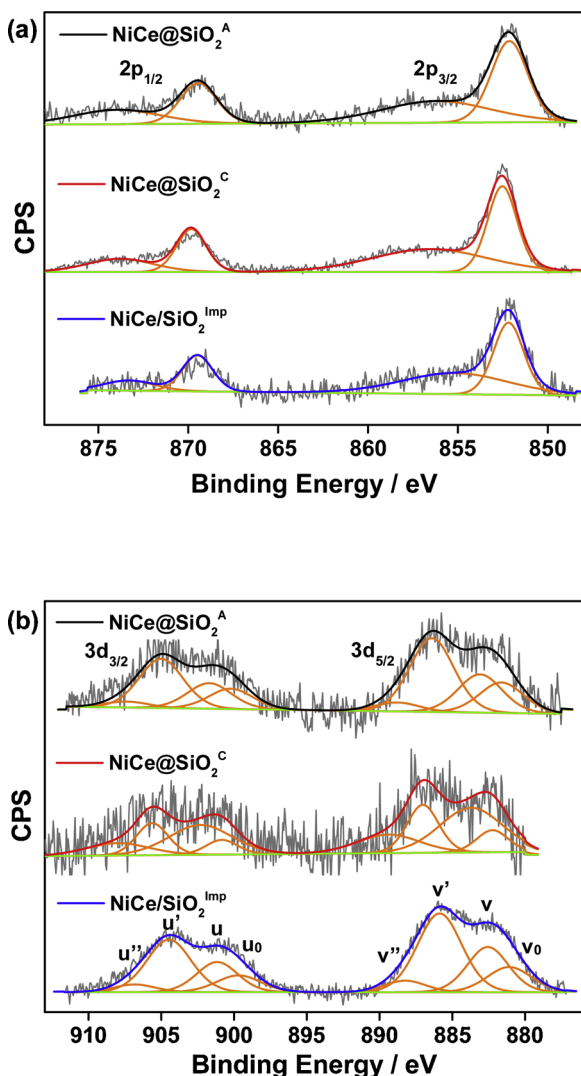


Fig. 5. (a) Ni 2p and (b) Ce 3d XPS spectra of reduced $\text{NiCe@SiO}_2^{\text{A}}$, $\text{NiCe@SiO}_2^{\text{C}}$, and $\text{NiCe/SiO}_2^{\text{Imp}}$.

the Ni 2p core level spectra of the reduced $\text{NiCe@SiO}_2^{\text{A}}$, $\text{NiCe@SiO}_2^{\text{C}}$, and $\text{NiCe/SiO}_2^{\text{Imp}}$ catalysts have characteristic metallic Ni peaks of Ni 2p_{3/2} (852.2 eV) and Ni 2p_{1/2} (869.5 eV) accompanied by shake-up structures [35,46]. Fig. 5 (b) shows the Ce 3d core level XPS spectra of the reduced samples. The Ce core level spectra can be deconvoluted into multiple peaks for Ce 3d_{5/2} (v) and Ce 3d_{3/2} (u). The v and v' bands are attributed to Ce^{4+} , whereas v₀ and v' bands are assigned to Ce^{3+} . The other bands (v'' and u'') available for Ce could not be detected due to the low signal-to-noise ratio. The relative Ce^{3+} concentration on the catalyst is calculated by the ratio of integrated Ce^{3+} peaks to the total Ce^{3+} and Ce^{4+} peaks ($\text{Ce}^{3+}/(\text{Ce}^{3+} + \text{Ce}^{4+})$). It has been found that $\text{NiCe/SiO}_2^{\text{Imp}}$ has the highest Ce^{3+} concentration of 62.9% followed by 61.6% and 36.1% for $\text{NiCe@SiO}_2^{\text{A}}$ and $\text{NiCe@SiO}_2^{\text{C}}$, respectively (Table 3). This shows that more oxygen vacancies formed in the CeO_2 lattice by the dispersed NiO particles in $\text{NiCe/SiO}_2^{\text{Imp}}$ and aggregated NiO yolk in $\text{NiCe@SiO}_2^{\text{A}}$.

3.2. TRM activity

The experiments for TRM were carried out at different O/M feed ratios to determine the activity and stability of the multi-yolk-shell nanotube and impregnated catalysts. Fig. 6 (a) and (b) illustrate CO_2 and CH_4 conversions at 750 °C at O/M feed ratios of 1.1 and 1.0, respectively. As shown in Fig. 6 (a), $\text{NiCe@SiO}_2^{\text{A}}$ and $\text{NiCe/SiO}_2^{\text{Imp}}$ have

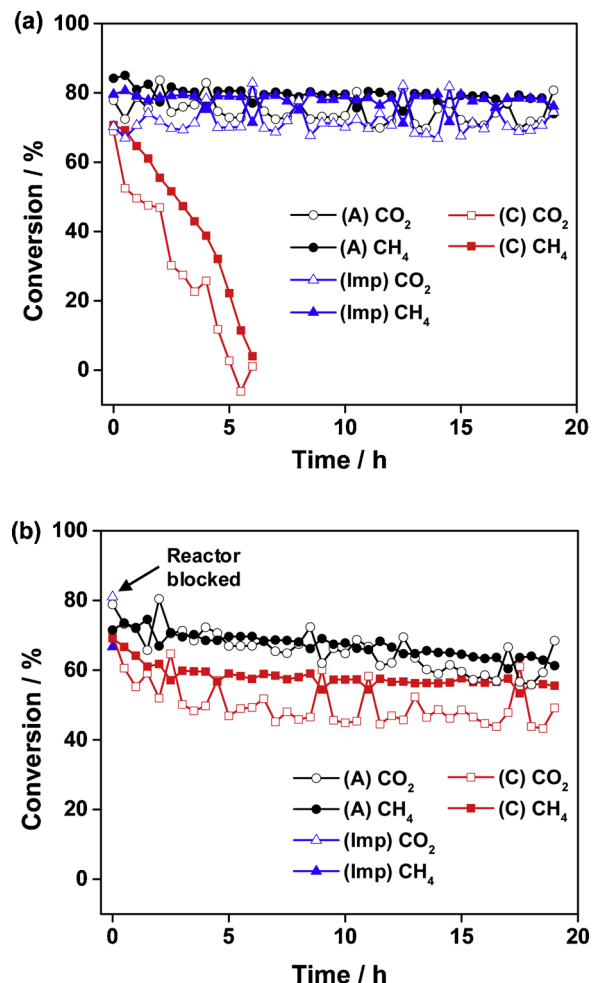


Fig. 6. CO_2 and CH_4 conversions of (A) $\text{NiCe@SiO}_2^{\text{A}}$, (C) $\text{NiCe@SiO}_2^{\text{C}}$, and (Imp) $\text{NiCe/SiO}_2^{\text{Imp}}$ catalysts at oxidizer to methane (O/M) ratios of (a) 1.1 and (b) 1.0 feed stream at 750 °C. The thermodynamic equilibrium conversions of CO_2 and CH_4 are 75.9% and 92.8% for O/M of 1.1 and 81.1% and 89.6% for O/M of 1.0, respectively.

comparable CO_2 conversions of 75% and 72%, and CH_4 conversions of 79% and 78% at O/M ratio of 1.1, respectively. $\text{NiCe@SiO}_2^{\text{A}}$ and $\text{NiCe/SiO}_2^{\text{Imp}}$ present H_2 and CO yields of 75% and 77%, and 79% and 72% with the same H_2/CO ratio of 1.7, respectively (Fig. S6). Both catalysts keep their activities stable over the 20 h period of reaction. In contrast, $\text{NiCe@SiO}_2^{\text{C}}$ shows an initial CO_2 and CH_4 conversions of 69% and 71%, respectively, yet both CO_2 and CH_4 conversions drop to below 5% within about 5 h. TRM activity of $\text{NiCe@SiO}_2^{\text{A}}$ with larger yolks was further tested at a higher O/M feed ratio of 1.25 to examine the catalytic activity and potential deactivation of the catalyst (Fig. S7). The result shows that the $\text{NiCe@SiO}_2^{\text{A}}$ catalyst still presents a stable activity with conversions of 67% and 84% for CO_2 and CH_4 , respectively. As the O/M feed ratio decreases to 1.0, the catalysts show distinctive behavior compared to those tested at the O/M feed ratio of 1.1. As shown in Fig. 6 (b), $\text{NiCe@SiO}_2^{\text{A}}$ and $\text{NiCe@SiO}_2^{\text{C}}$ have CO_2 conversions of 66% and 50%, and CH_4 conversions of 67% and 58%, respectively. For $\text{NiCe@SiO}_2^{\text{A}}$, these conversions correspond to the H_2 and CO yields of 68% and 64% with a H_2/CO ratio of 1.8 (Fig. S6). The conventional $\text{NiCe/SiO}_2^{\text{Imp}}$ starts with similar conversion as the multi-yolk-shell nanotube catalysts, however, the conversions plummet after about 1 h (Fig. 6 (b)). The fast deactivation of $\text{NiCe/SiO}_2^{\text{Imp}}$ can be attributed to severe carbon formation, which has blocked the catalyst bed. The higher resistance to carbon deposition for the multi-yolk-shell catalyst than impregnated catalyst might come from the strong metal-support

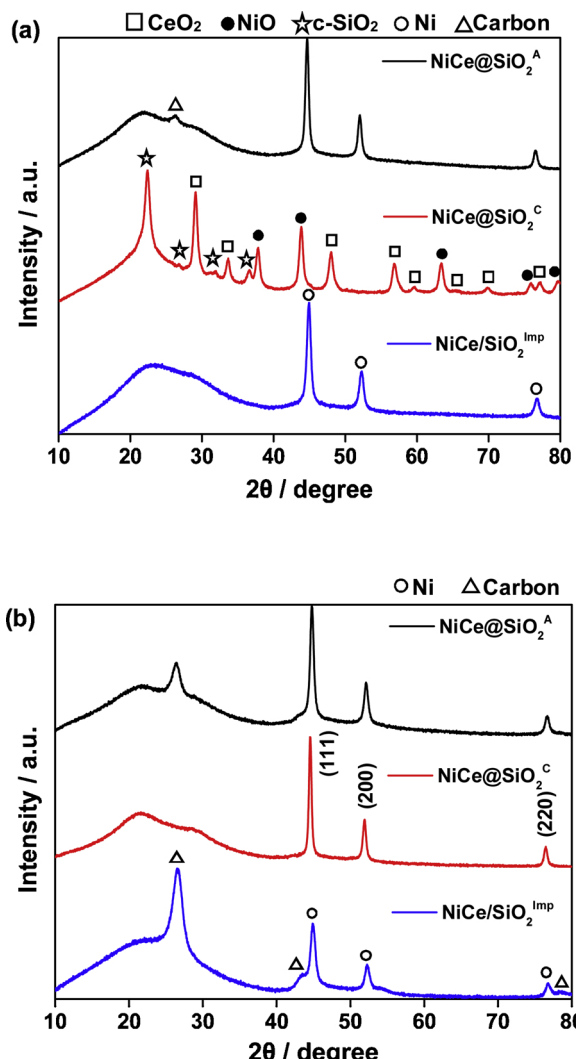


Fig. 7. XRD patterns for spent catalysts of NiCe@SiO₂^A, NiCe@SiO₂^C, and NiCe/SiO₂^{Imp} after the TRM reaction in O/M ratios of (a) 1.1 and (b) 1.0 feed stream at 750 °C.

interaction due to confinement effect [66]. Both lower conversion and yield measured under reducing condition ($O/M = 1.0$) than oxidizing condition ($O/M = 1.1$) can be explained by the side reactions (reactions (8–10) and (12)) which facilitate carbon deposition [67]. Most of the carbon can be deposited on the catalyst by methane cracking reaction (8) at 750 °C, leading to the increase in H_2/CO ratio [55].

3.3. Characterization of the spent catalysts

Fig. 7 (a) and (b) show the XRD spectra of the spent catalysts after TRM at the O/M feed ratio of 1.1 and 1.0, respectively. The XRD measurements performed on the spent catalysts after the TRM at the O/M feed ratio of 1.1 indicate that the reduced metallic Ni ($2\theta = 44.7^\circ$, 52.0° , and 76.6°) and amorphous SiO₂ shell maintained its phase in the NiCe@SiO₂^A and NiCe/SiO₂^{Imp} catalysts (Fig. 7 (a)). No CeO₂ peaks are observed on NiCe@SiO₂^A and NiCe/SiO₂^{Imp} after the reaction because crystalline CeO₂ phase turned into the amorphous phase in the presence of H₂ at temperatures above 600 °C [59,68,69]. Despite the change of Ni and Ce phases during the reaction, the TEM image of the spent NiCe@SiO₂^A shows that the morphology of the multi-yolk-shell nanotube is preserved without collapsing, as shown in Fig. 8 (a). Further testing of NiCe@SiO₂^A at a higher O/M feed ratio of 1.25 also shows that higher oxidizer concentration in the feed stream does not influence the NiCe@

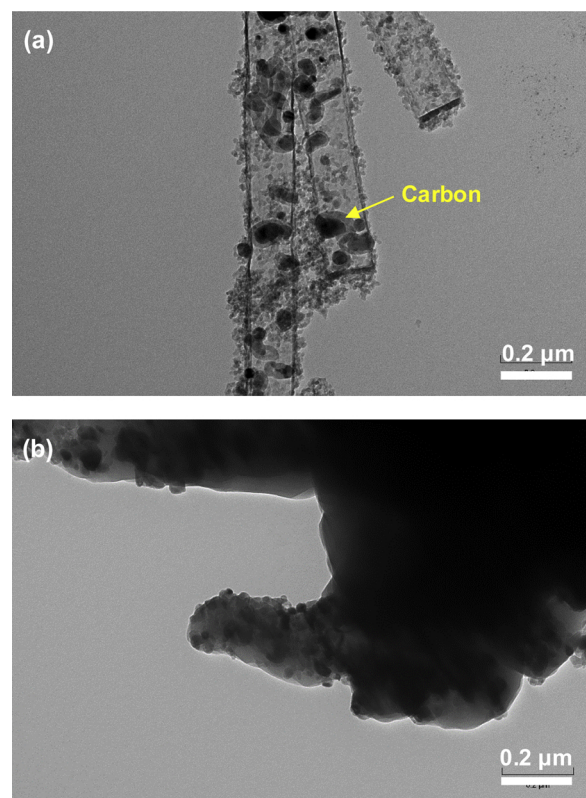


Fig. 8. TEM images of spent (a) NiCe@SiO₂^A and (b) NiCe@SiO₂^C after 20 h of TRM in O/M ratio of 1.1 feed stream.

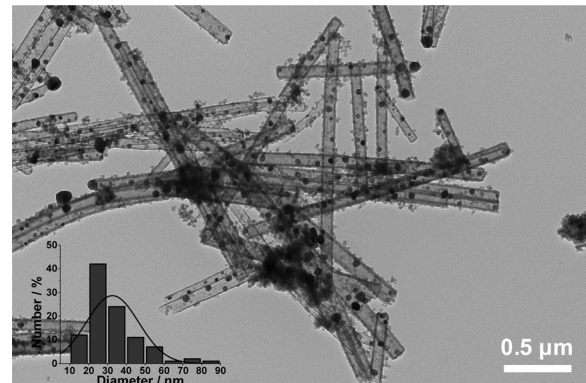


Fig. 9. TEM image of spent NiCe@SiO₂^A after 20 h of TRM in O/M ratio of 1.25 feed stream. Inset graph shows yolk size distribution.

SiO₂^A catalyst morphology (Fig. 9). The mean yolk size of the spent catalyst (32.7 nm) is similar to the size of the fresh catalyst (32.9 nm). These results show that yolks are not likely to sinter during the reaction due to the strong interaction between the metal yolk and the silica shell [70,71]. However, in the case of NiCe@SiO₂^C, crystalline phases of NiO, CeO₂ and SiO₂ are observed for the spent catalyst due to re-oxidation at O/M ratio of 1.1 during the TRM (Fig. 7 (a)). The deactivation of NiCe@SiO₂^C is likely caused by oxidation of the active metallic Ni, followed by destruction of the multi-yolk-shell nanotube structure (Fig. 8 (b)). Fig. S8 shows the diffraction pattern of NiCe@SiO₂^C analyzed during the deactivation process. Both metallic Ni and Ni²⁺ phases are detected after 3 h of TRM, indicating that fully reduced Ni phase starts to be oxidized to the NiO phase at high O/M feed ratio, leading to the deactivation of the catalyst. It is important to note that a high amount of oxidizing species in the feed stream can still lead to the formation of carbon on the NiCe@SiO₂^A catalyst. As shown in the

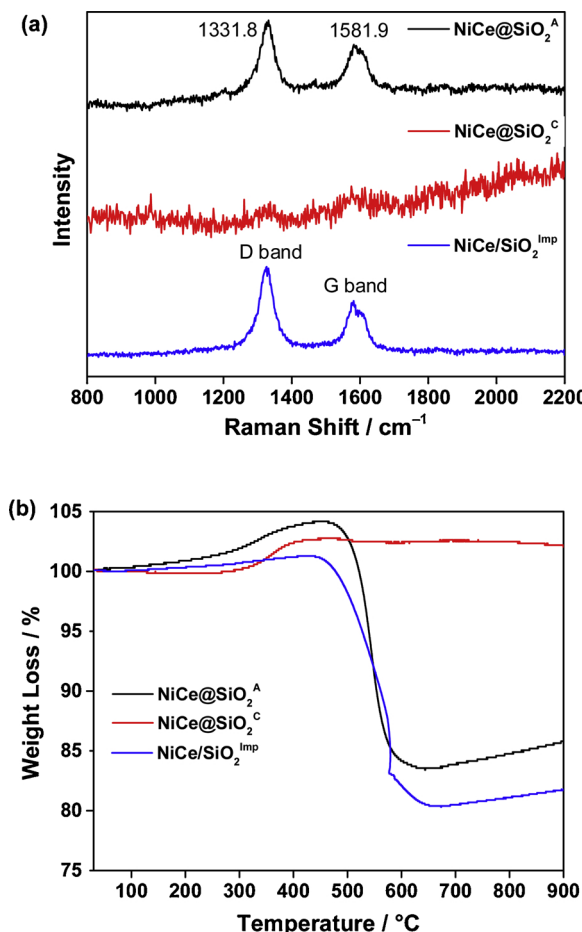


Fig. 10. (a) Raman spectra and (b) TGA profiles for spent catalysts of NiCe@SiO₂^A, NiCe@SiO₂^C, and NiCe/SiO₂^{imp} after the TRM reaction in O/M ratio of 1.0 feed stream.

diffraction pattern of the spent NiCe@SiO₂^A (Fig. 7 (a)), carbon is detected at a two-theta of 26.6° [17,18]. The carbon deposition can also be observed in the TEM image of the spent catalyst (Fig. 8 (a)). Our results suggest that carbon deposition on the spent NiCe@SiO₂^A is not high enough to affect the stability of the catalyst.

The XRD spectra of the spent catalysts after TRM at the O/M feed ratio of 1.0 show that all three catalysts have metallic Ni peaks along with wide amorphous SiO₂ peak, as shown in Fig. 7 (b). Similarly, CeO₂ turns to the amorphous phase and its diffraction peaks are not observed on all three spent catalysts after the reaction. The spent NiCe/SiO₂^{imp} catalyst has much stronger intensity for carbon peak at 26.6° than NiCe@SiO₂^A, while no carbon peak is detected for NiCe@SiO₂^C after 20 h of the TRM reaction. These results suggest that the multi-yolk-shell nanotube catalyst with smaller yolks presents high resistance to carbon deposition providing longer stability for TRM at the O/M feed ratio of 1.0. Raman spectra of the spent NiCe@SiO₂^A, NiCe@SiO₂^C, and NiCe/SiO₂^{imp} catalysts after the reaction at O/M feed ratio of 1.0 were collected to determine the nature of carbon formed on the spent catalyst. As shown in Fig. 10 (a), both the spent NiCe@SiO₂^A and NiCe/SiO₂^{imp} catalysts have carbon formations, in agreement with the XRD measurement, while carbon peaks are barely seen for NiCe@SiO₂^C after 20 h of TRM. The two bands observed at 1331.8 cm⁻¹ and 1581.9 cm⁻¹ on the spent NiCe@SiO₂^A and NiCe/SiO₂^{imp} catalysts can be ascribed to carbon sp² bonds in which the first peak is assigned to the D band with defects or amorphous carbon, while the second peak belongs to the G band with ordered graphite structure [46]. TGA was performed to quantify the amount of carbon deposited on the spent catalysts after the reaction. As shown in Fig. 10 (b), the weight of the spent

multi-yolk-shell nanotube catalysts slightly increases starting from 260 °C due to oxidation of the catalyst. The sample weight loss occurs at temperatures between 450 °C and 650 °C for NiCe@SiO₂^A and NiCe@SiO₂^{imp} due to the gasification of the carbon formed during the TRM reaction. The deposited carbon amount is calculated to be 0.16 mg g_{cat}⁻¹ and 0.20 mg g_{cat}⁻¹ for NiCe@SiO₂^A and NiCe@SiO₂^{imp}, respectively. In consistent with the XRD and Raman analysis, the weight of NiCe@SiO₂^C remains constant at temperatures between 450 °C and 900 °C, indicating that carbon species are not likely to form on the catalyst during 20 h of TRM. The high resistance to carbon deposition of NiCe@SiO₂ multi-yolk-shell nanotube catalysts can be possibly due to the strong binding of active Ni species to SiO₂, as illustrated in the H₂-TPR data. It is also possible that the unique morphology of the multi-yolk-shell nanotube structures does not allow carbon to be deposited on the active sites due to the confinement effect. Despite the unique morphology of the multi-yolk-shell nanotube catalysts, the XRD, Raman, and TGA results confirm that carbon can still form on larger yolks (NiCe@SiO₂^A), while smaller yolks (NiCe@SiO₂^C) exhibit higher resistance to carbon deposition at the O/M ratio of 1.0 feed stream.

3.4. Effect of yolk size under reducing conditions

To understand the effect of yolk size on TRM activity, NiCe@SiO₂^B with a mean yolk size between NiCe@SiO₂^A and NiCe@SiO₂^C was synthesized and three multi-yolk-shell nanotube catalysts were evaluated at much higher methane concentration with an O/M feed ratio of 0.85. As shown in Fig. 11, NiCe@SiO₂^C with a mean yolk size of 20.0 nm still presents a stable activity with CO₂ and CH₄ conversions of 73% and 61%, respectively. However, the NiCe@SiO₂^A catalyst with the largest yolks deactivates within 2 h by carbon formation. NiCe@SiO₂^B with a mean yolk size of 23.7 nm shows slightly longer stability than NiCe@SiO₂^A, but the catalyst also loses its activity in 4 h due to the blockage of the catalyst bed by carbon formation. As shown in Fig. S9, carbon peaks in XRD are detected for both of the spent NiCe@SiO₂^A and NiCe@SiO₂^C catalysts, but NiCe@SiO₂^A with larger yolks have stronger carbon peak intensity than NiCe@SiO₂^C with smaller yolks after the reaction with the O/M feed ratio of 0.85. Throughout the three multi-yolk-shell nanotube catalysts tested, NiCe@SiO₂^C exhibits the most stable activity at both O/M ratio of 1.0 and 0.85 due to the fast carbon removal reaction, whereas the other catalysts with mean yolk size larger than 20.0 nm (NiCe@SiO₂^A and NiCe@SiO₂^B) deactivate at high CH₄ concentration feed streams.

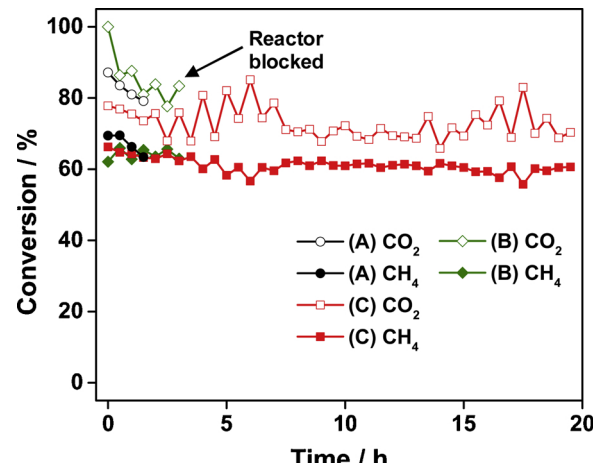
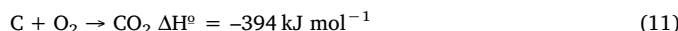
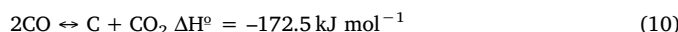
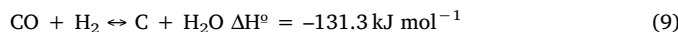
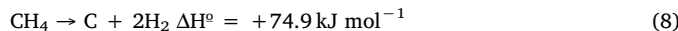


Fig. 11. CO₂ and CH₄ conversions of (A) NiCe@SiO₂^A, (B) NiCe@SiO₂^B, and (C) NiCe@SiO₂^C at 750 °C in O/M ratio of 0.85 feed stream. Under this condition, the thermodynamic equilibrium conversions of CO₂ and CH₄ are 89.0% and 83.0%, respectively.



During the TRM reaction, carbon formation can occur via the following reactions: methane cracking (8), reduction of CO (9), and the Boudouard reaction (10). At the same time, the deposited carbon can be removed by the reverse reactions of (9) and (10), and the forward reaction of (11), in which carbon reacts with H_2O , CO_2 and O_2 , respectively. While these reactions occur simultaneously on the catalyst, carbon formation and removal reaction rates can be influenced by the Ni particle size. Different Ni particle sizes ranging in between 6 nm and 26 nm have been reported for the net formation of carbon on Ni-based catalyst [72–74]. It has been shown that the removal rate of carbon is faster than the formation rate of carbon on catalysts containing smaller Ni particles, indicating that large Ni particles are more susceptible to carbon formation [73,75]. In particular, the carbon formation rate in SRM is found to be directly related to the Ni particle size with smaller Ni particles resulting in a lower coking rate due to the low driving force for carbon diffusion through the Ni [76]. In addition to the carbon formation rates, smaller Ni particles are shown to yield carbon filaments with smaller diameters in DRM compared to filaments formed on larger Ni particles [77]. Growth of smaller diameter carbon filaments is not thermodynamically favorable, resulting in less carbon deposition compared to larger diameter carbon filaments. Carbon filament growth can be related to the equilibrium Gibbs free energy growth of graphite. Deviations from graphite's equilibrium Gibbs free energy are inversely proportional to particle diameter. The deviations from the graphite equilibrium value represent extra energy needed by the system to form filamentous carbon, therefore smaller Ni particles lead to larger deviations resulting in less carbon filament growth [78]. In POM, smaller Ni particles result in the formation of more hydrogen containing carbon species than graphitic or nanotube structure carbon [79]. Carbon species containing hydrogen are easily gasified and therefore do not cause catalyst deactivation, meaning that smaller particles are not as easily deactivated by carbon as larger particles. It stands to reason that the catalyst containing smaller yolks might form less and more easily removable carbon than the catalyst containing larger yolks. However, no distinctive conclusion can be made in terms of what Ni particle size is more beneficial to prevent carbon formation, as it highly depends on the chemistry and morphology of the catalyst. In addition to the Ni yolk size, Ni–Ce interaction can play a major role on the stability of the catalyst. Under reducing conditions i.e., O/M feed ratios of 0.85 and 1.0, $\text{NiCe@SiO}_2^{\text{C}}$ has high resistance to carbon deposition possibly due to the high amount of Ce^{4+} concentration. The first step in methane reforming reactions is believed to start with CH_4 dissociation to generate hydrocarbon species and carbon atoms [80]. Carbon atoms can be oxidized by reacting with CO_2 (reaction (10)) and Ce^{4+} (reaction (12)). The reverse reaction of (12) could be observed for the $\text{NiCe@SiO}_2^{\text{A}}$ and $\text{NiCe/SiO}_2^{\text{Imp}}$ catalysts as they have high Ce^{3+} concentration, thereby can produce more carbon deposits compared to $\text{NiCe@SiO}_2^{\text{C}}$ [80].

3.5. Effect of yolk size under oxidizing conditions

The active metallic Ni phase in small yolks can be re-oxidized by adsorbing oxygen species from the feed gases or interaction with CeO_2 at O/M feed ratios higher than 1.0. Large Ni yolks can have slower carbon removal rate leading to carbon deposition even at higher O/M ratios feed stream, as shown in Fig. 7 (a) and Fig. 8 (a). However, it has been hypothesized that the carbon formation on large Ni particles can

prevent Ni metal from being oxidized in the high oxygen-containing feed stream (O/M ratio > 1.0) [81]. On the other hand, carbon formation rate is slower than the carbon oxidation rate on the small yolks ($\text{NiCe@SiO}_2^{\text{C}}$), therefore, the amount of deposited carbon may not be sufficient enough to prevent the oxidation of metallic Ni to NiO , leading to deactivation of the catalyst. In contrast to the NiCe@SiO_2 multi-yolk-shell nanotube catalyst, the conventional $\text{NiCe/SiO}_2^{\text{Imp}}$ catalyst exhibits stable activity without both Ni oxidation and carbon formation confirmed by XRD at the O/M feed ratio of 1.1 (Fig. 7 (a)). This can be explained by the fact that $\text{NiCe/SiO}_2^{\text{Imp}}$ has stronger interaction between dispersed Ni and Ce species confirmed by $\text{H}_2\text{-TPR}$ and XPS. The $\text{Ce}^{3+}/\text{Ce}^{4+}$ redox property on CeO_2 provides high surface and bulk oxygen vacancies [29]. Therefore, it is possible that the oxygen species migrate to the oxygen vacancies on CeO_2 , which hinders Ni species from being oxidized. The stable activity of $\text{NiCe@SiO}_2^{\text{A}}$ and $\text{NiCe/SiO}_2^{\text{Imp}}$ at O/M ratio of 1.1 can also be explained by Ce effect as aggregated Ni yolks and dispersed Ni particles in interaction with Ce lead to the formation of more Ce^{3+} species evidenced by $\text{H}_2\text{-TPR}$ and XPS. Availability of Ce^{3+} and Ce^{4+} species can shift the equilibrium of the reaction (13) and facilitate Ni oxidation [80]. Both $\text{NiCe@SiO}_2^{\text{A}}$ and $\text{NiCe/SiO}_2^{\text{Imp}}$ have higher Ce^{3+} concentration compared to $\text{NiCe@SiO}_2^{\text{C}}$ and show stable activity without Ni oxidation. On the contrary, the forward reaction of (13) can be observed for the $\text{NiCe@SiO}_2^{\text{C}}$ as it has high Ce^{4+} concentration, thereby can oxidize active Ni yolks.

In summary, our results indicate that carbon formation and removal rates need to be balanced to obtain stable performance under the TRM by controlling the Ni yolk size and Ni–Ce interaction. If the carbon formation is faster than carbon removal process, the carbon will deposit onto the catalyst, whereas if the carbon removal reaction rate is faster than carbon formation rate, the metallic Ni species can be oxidized to NiO by exposing to oxygen species, which both cases can deactivate the catalyst [82,83]. While the effect of yolk size and Ce effect on the TRM activity can be pronounced, other structural parameters, such as shell thickness and tube diameter of the multi-yolk-shell nanotube catalysts, should be systematically analyzed in future studies.

4. Conclusions

Different morphologies of NiCe@SiO_2 multi-yolk-shell nanotube catalysts were synthesized by controlling the water to surfactant ratio in the reverse microemulsion method. The multi-yolk-shell nanotube catalyst prepared at a high water/surfactant ratio forms smaller yolks surrounded by a longer diameter silica tube shell, whereas a low water/surfactant ratio produces larger yolks with a shorter diameter tube shell. Catalysts prepared with small and large yolks show distinct characteristic behavior at various feed gas ratios under TRM. At a low O/M feed ratio, the NiCe@SiO_2 multi-yolk-shell nanotube catalysts exhibit high resistance to carbon deposition due to its confinement effect. In contrast, the conventional $\text{NiCe/SiO}_2^{\text{Imp}}$ catalyst produces a high amount of carbon deposition on the catalyst, which deactivates the catalyst fast. The NiCe@SiO_2 multi-yolk-shell nanotube catalyst with smaller yolks forms less carbon compared to the catalyst with larger yolk sizes (> 20 nm) possibly due to the facile oxidation of carbon on the smaller Ni yolks and low Ce^{3+} concentration. On the other hand, at a high O/M feed ratio, the NiCe@SiO_2 catalyst containing smaller yolks tends to be easily re-oxidized by oxygen species leading to the catalyst deactivation followed by destruction of multi-yolk-shell nanotube morphology. However, the NiCe@SiO_2 with larger yolks shows stable activity without oxidation possibly due to the slower carbon removal reaction rate and high Ce^{3+} concentration. Our results show that the morphology of the NiCe@SiO_2 multi-yolk-shell nanotube catalysts will influence the TRM activity at different O/M feed ratios, and this tunable morphology can be engineered for obtaining high TRM activity and stability.

Declaration of Competing Interests

The authors declare that they have no known competing financial interests or personal relationships that could have appeared to influence the work reported in this paper.

Acknowledgements

This research was performed, in part, using instrumentation (FEI Talos F200X S/TEM) provided by the Department of Energy, Office of Nuclear Energy, Fuel Cycle R&D Program and the Nuclear Science User Facilities. We acknowledge funding from the South Carolina Smartstate Center for Strategic Approaches to the Generation of Electricity (SAGE).

Appendix A. Supplementary data

Supplementary material related to this article can be found, in the online version, at doi:<https://doi.org/10.1016/j.apcatb.2019.118037>.

References

- [1] D.A. Lashof, D.R. Ahuja, Relative contributions of greenhouse gas emissions to global warming, *Nature*. 344 (1990) 529–531, <https://doi.org/10.1038/344529a0>.
- [2] C. Song, Global challenges and strategies for control, conversion and utilization of CO₂ for sustainable development involving energy, catalysis, adsorption and chemical processing, *Catal. Today* 115 (2006) 2–32, <https://doi.org/10.1016/j.cattod.2006.02.029>.
- [3] R. Cassia, M. Nocioni, N. Correa-Aragunde, L. Lamattina, Climate change and the impact of greenhouse gasses: CO₂ and NO_x, friends and foes of plant oxidative stress, *Front. Plant Sci.* 9 (2018) 1–11, <https://doi.org/10.3389/fpls.2018.00273>.
- [4] A. Omri, CO₂emissions, energy consumption and economic growth nexus in MENA countries: Evidence from simultaneous equations models, *Energy Econ.* 40 (2013) 657–664, <https://doi.org/10.1016/j.eneco.2013.09.003>.
- [5] C. Ampelli, S. Perathoner, G. Centi, CO₂ utilization: an enabling element to move to a resource- and energy-efficient chemical and fuel production, *Philos. Trans. Math. Phys. Eng. Sci.* 373 (2015) 20140177, , <https://doi.org/10.1098/rsta.2014.0177>.
- [6] S. Saeidi, N.A.S. Amin, M.R. Rahimpour, Hydrogenation of CO₂to value-added products—a review and potential future developments, *J. CO₂ Util* 5 (2014) 66–81, <https://doi.org/10.1016/j.jcou.2013.12.005>.
- [7] D.T. Whipple, P.J.A. Kenis, Prospects of CO₂ utilization via direct heterogeneous electrochemical reduction, *J. Phys. Chem. Lett.* 1 (2010) 3451–3458, <https://doi.org/10.1021/jz1012627>.
- [8] K.M.K. Yu, I. Curcic, J. Gabriel, S.C.E. Tsang, Recent advances in CO₂ capture and utilization, *ChemSusChem*. 1 (2008) 893–899, <https://doi.org/10.1002/cssc.200800169>.
- [9] Z. Jiang, T. Xiao, V.L. Kuznetsov, P.P. Edwards, Turning carbon dioxide into fuel, *Philos. Trans. R. Soc. A Math. Phys. Eng. Sci.* 368 (2010) 3343–3364, <https://doi.org/10.1098/rsta.2010.0119>.
- [10] H.-J. Freund, M.W. Roberts, Surface chemistry of carbon dioxide, *Surf. Sci. Rep.* 25 (1996) 225–273, [https://doi.org/10.1016/S0167-5729\(96\)00007-6](https://doi.org/10.1016/S0167-5729(96)00007-6).
- [11] C. Song, W. Pan, Tri-reforming of methane: a novel concept for catalytic production of industrially useful synthesis gas with desired H₂/CO ratios, *Catal. Today* 98 (2004) 463–484, <https://doi.org/10.1016/j.cattod.2004.09.054>.
- [12] J.S. Kang, D.H. Kim, S.D. Lee, S.I. Hong, D.J. Moon, Nickel-based tri-reforming catalyst for the production of synthesis gas, *Appl. Catal. A-Gen.* 332 (2007) 153–158, <https://doi.org/10.1016/j.apcata.2007.08.017>.
- [13] M. Sadeghi, M. Jafari, M. Yari, S.M.S. Mahmoudi, Exergoeconomic assessment and optimization of a syngas production system with a desired H₂/CO ratio based on methane tri-reforming Process, *J. CO₂ Util* 25 (2018) 283–301, <https://doi.org/10.1016/j.jcou.2018.04.009>.
- [14] X. Zhao, D.M. Walker, D. Maiti, A.D. Petrov, M. Kastelic, B. Joseph, J.N. Kuhn, NiMg/ceria-zirconia cylindrical pellet catalysts for tri-reforming of surrogate biogas, *Ind. Eng. Chem. Res.* 57 (2018) 845–855, <https://doi.org/10.1021/acs.iecr.7b03669>.
- [15] M. Minutillo, A. Perna, A novel approach for treatment of CO₂ from fossil fired power plants, Part A: the integrated systems ITRPP, *Int. J. Hydrogen Energy* 34 (2009) 4014–4020, <https://doi.org/10.1016/j.ijhydene.2009.02.069>.
- [16] C. Pichas, P. Pomonis, D. Petrakias, A. Ladavos, Kinetic study of the catalytic dry reforming of CH₄ with CO₂ over La_{2-x}Sr_xNiO₄ perovskite-type oxides, *Appl. Catal. A-Gen.* 386 (2010) 116–123, <https://doi.org/10.1016/j.apcata.2010.07.043>.
- [17] L. Guczi, G. Stefler, O. Geszti, I. Sajó, Z. Pászti, A. Tompos, Z. Schay, Methane dry reforming with CO₂: a study on surface carbon species, *Appl. Catal. A-Gen.* 375 (2010) 236–246, <https://doi.org/10.1016/j.apcata.2009.12.040>.
- [18] I.H. Son, S.J. Lee, I.Y. Song, W.S. Jeon, I. Jung, D.J. Yun, D.W. Jeong, J.O. Shim, W.J. Jang, H.S. Roh, Study on coke formation over Ni/γ-Al₂O₃, Co-Ni/γ-Al₂O₃, and Mg-Co-Ni/γ-Al₂O₃ catalysts for carbon dioxide reforming of methane, *Fuel*. 136 (2014) 194–200, <https://doi.org/10.1016/j.fuel.2014.07.041>.
- [19] X. Zhao, M. Lu, H. Li, J. Fang, L. Shi, D. Zhang, In situ preparation of Ni nanoparticles in cerium-modified silica aerogels for coking- and sintering-resistant dry reforming of methane, *New J. Chem.* 41 (2017) 4869–4878, <https://doi.org/10.1039/c7nj00115k>.
- [20] S.H. Lee, W. Cho, W.S. Ju, B.H. Cho, Y.C. Lee, Y.S. Baek, Tri-reforming of CH₄ using CO₂ for production of synthesis gas to dimethyl ether, *Catal. Today* 87 (2003) 133–137, <https://doi.org/10.1016/j.cattod.2003.10.005>.
- [21] A. Dwivedi, R. Gudi, P. Biswas, An improved tri-Reforming based methanol production process for enhanced CO₂ valorization, *Int. J. Hydrogen Energy* 42 (2017) 23227–23241, <https://doi.org/10.1016/j.ijhydene.2017.07.166>.
- [22] W.L. Luyben, Control of parallel dry methane and steam methane reforming processes for Fischer-Tropsch syngas, *J. Process Control* 39 (2016) 77–87, <https://doi.org/10.1016/j.jprocont.2015.11.007>.
- [23] Z. Bian, Z. Wang, S. Kawi, Ni-phyllosilicate structure derived Ni-SiO₂-MgO catalysts for bi-reforming applications: acidity, basicity and thermal stability, *Catal. Sci. Technol.* 8 (2018) 1730–1742, <https://doi.org/10.1039/c7cy02475d>.
- [24] Y. Kathiraser, Z. Wang, M.L. Ang, L. Mo, Z. Li, U. Oemar, S. Kawi, Highly active and coke resistant Ni/SiO₂catalysts for oxidative reforming of model biogas: Effect of low ceria loading, *J. CO₂ Util* 19 (2017) 284–295, <https://doi.org/10.1016/j.jcou.2017.03.018>.
- [25] R.K. Singha, A. Shukla, A. Yadav, S. Adak, Z. Iqbal, N. Siddiqui, R. Bal, Energy efficient methane tri-reforming for synthesis gas production over highly coke resistant nanocrystalline Ni-ZrO₂ catalyst, *Appl. Energy* 178 (2016) 110–125, <https://doi.org/10.1016/j.apenergy.2016.06.043>.
- [26] Y. Zhang, S. Zhang, J.L. Gossage, H.H. Lou, T.J. Benson, Thermodynamic analyses of tri-reforming reactions to produce syngas, *Energy Fuels* 28 (2014) 2717–2726, <https://doi.org/10.1021/ef500084m>.
- [27] J.M. García-Vargas, J.L. Valverde, J. Díez, F. Dorado, P. Sánchez, Catalytic and kinetic analysis of the methane tri-reforming over a Ni-Mg/β-SiC catalyst, *Int. J. Hydrogen Energy* 40 (2015) 8677–8687, <https://doi.org/10.1016/j.ijhydene.2015.05.032>.
- [28] M. Schmal, F.S. Toniolo, C.E. Kozono, Perspective of catalysts for (Tri) reforming of natural gas and flue gas rich in CO₂, *Appl. Catal. A-Gen.* 568 (2018) 23–42, <https://doi.org/10.1016/j.apcata.2018.09.017>.
- [29] S. Wang, G.Q. Lu, Role of CeO₂ in Ni/CeO₂-Al₂O₃ catalysts for carbon dioxide reforming of methane, *Appl. Catal. B-Environ.* 19 (1998) 267–277, [https://doi.org/10.1016/S0926-3373\(98\)00081-2](https://doi.org/10.1016/S0926-3373(98)00081-2).
- [30] F. Deganello, A. Martorana, Phase analysis and oxygen storage capacity of ceria-lanthana-based TWC promoters prepared by sol-gel routes, *J. Solid State Chem.* 163 (2002) 527–533, <https://doi.org/10.1006/jssc.2001.9442>.
- [31] J.B. Wang, Y.L. Tai, W.P. Dow, T.J. Huang, Study of ceria-supported nickel catalyst and effect of yttria doping on carbon dioxide reforming of methane, *Appl. Catal. A-Gen.* 218 (2001) 69–79, [https://doi.org/10.1016/S0926-860X\(01\)00620-2](https://doi.org/10.1016/S0926-860X(01)00620-2).
- [32] L. Pino, A. Vita, F. Cipiti, M. Lagamà, V. Recupero, Hydrogen production by methane tri-reforming process over Ni-ceria catalysts: effect of La-doping, *Appl. Catal. B-Environ.* 104 (2011) 64–73, <https://doi.org/10.1016/j.apcatb.2011.02.027>.
- [33] J.M. García-Vargas, J.L. Valverde, J. Díez, P. Sánchez, F. Dorado, Preparation of Ni-Mg/β-SiC catalysts for the methane tri-reforming: effect of the order of metal impregnation, *Appl. Catal. B-Environ.* 164 (2015) 316–323, <https://doi.org/10.1016/j.apcatb.2014.09.044>.
- [34] D.M. Walker, S.L. Pettit, J.T. Wolan, J.N. Kuhn, Synthesis gas production to desired hydrogen to carbon monoxide ratios by tri-reforming of methane using Ni-Mg-(Ce,Zr)O₂ catalysts, *Appl. Catal. A-Gen.* 445–446 (2012) 61–68, <https://doi.org/10.1016/j.apcata.2012.08.015>.
- [35] R.K. Singha, S. Das, M. Pandey, S. Kumar, R. Bal, A. Bordoloi, Ni nanocluster on modified CeO₂-ZrO₂ nanoporous composite for tri-reforming of methane, *Catal. Sci. Technol.* 6 (2016) 7122–7136, <https://doi.org/10.1039/C5CY01323B>.
- [36] Q. Yao, Z.H. Lu, Z. Zhang, X. Chen, Y. Lan, One-pot synthesis of core-shell Cu@SiO₂ nanospheres and their catalysis for hydrolytic dehydrogenation of ammonia borane and hydrazine borane, *Sci. Rep.* 4 (2014) 4–11, <https://doi.org/10.1038/srep07597>.
- [37] R. Ghosh Chaudhuri, S. Paria, Core/shell nanoparticles: classes, properties, synthesis mechanisms, characterization, and applications, *Chem. Rev.* 112 (2012) 2373–2433, <https://doi.org/10.1021/cr00449n>.
- [38] F. Wang, L. Xu, W. Shi, Syngas production from CO₂ reforming with methane over core-shell Ni@SiO₂catalysts, *J. CO₂ Util* 16 (2016) 318–327, <https://doi.org/10.1016/j.jcou.2016.09.001>.
- [39] Z. Li, M. Li, Z. Bian, Y. Kathiraser, S. Kawi, Design of highly stable and selective core/yolk-shell nanocatalysts—a review, *Appl. Catal. B-Environ.* 188 (2016) 324–341, <https://doi.org/10.1016/j.apcatb.2016.01.067>.
- [40] Z. Li, S. Das, P. Hongmanorom, N. Dewangan, M.H. Wai, S. Kawi, Silica-based micro- and mesoporous catalysts for dry reforming of methane, *Catal. Sci. Technol.* 8 (2018) 2763–2778, <https://doi.org/10.1039/c8cy00622a>.
- [41] Z. Bian, S. Kawi, Sandwich-like silica@Ni@silica multicore-shell catalyst for the low-temperature dry reforming of methane: confinement effect against carbon formation, *ChemCatChem.* 10 (2018) 320–328, <https://doi.org/10.1002/cctc.201701024>.
- [42] Z. Li, S. Kawi, Multi-Ni@Ni phyllosilicate hollow sphere for CO₂ reforming of CH₄: influence of Ni precursors on structure, sintering, and carbon resistance, *Catal. Sci. Technol.* 8 (2018) 1915–1922, <https://doi.org/10.1039/c8cy00024g>.
- [43] J. Ashok, M.L. Ang, S. Kawi, Enhanced activity of CO₂ methanation over Ni/CeO₂-ZrO₂ catalysts: influence of preparation methods, *Catal. Today* 281 (2017) 304–311, <https://doi.org/10.1016/j.cattod.2016.07.020>.
- [44] Z. Li, Y. Kathiraser, J. Ashok, U. Oemar, S. Kawi, Simultaneous tuning porosity and basicity of nickel@nickel – magnesium phyllosilicate core – shell catalysts for CO₂ reforming of CH₄, *Langmuir.* 30 (2014) 14694–14705, <https://doi.org/10.1021/la503340s>.
- [45] Z. Li, Y. Kathiraser, S. Kawi, Facile synthesis of high surface area yolk-shell Ni@Ni

- embedded SiO₂ via Ni phyllosilicate with enhanced performance for CO₂ reforming of CH₄, *ChemCatChem.* 7 (2015) 160–168, <https://doi.org/10.1002/cctc.201402673>.
- [46] X. Zhao, H. Li, J. Zhang, L. Shi, D. Zhang, Design and synthesis of NiCe@m-SiO₂ yolk-shell framework catalysts with improved coke- and sintering-resistance in dry reforming of methane, *Int. J. Hydrogen Energy* 41 (2016) 2447–2456, <https://doi.org/10.1016/j.ijhydene.2015.10.111>.
- [47] J. Liu, H.Q. Yang, F. Kleitz, Z.G. Chen, T. Yang, E. Strounina, G.Q. Lu, S.Z. Qiao, Yolk-shell hybrid materials with a periodic mesoporous organosilica shell: ideal nanoreactors for selective alcohol oxidation, *Adv. Funct. Mater.* 22 (2012) 591–599, <https://doi.org/10.1002/adfm.201101900>.
- [48] J. Liu, S.Z. Qiao, J.S. Chen, X.W. (David) Lou, X. Xing, G.Q. (Max) Lu, Yolk/shell nanoparticles: new platforms for nanoreactors, drug delivery and lithium-ion batteries, *Chem. Commun. (Camb.)* 47 (2011) 12578–12591, <https://doi.org/10.1039/c1cc13658e>.
- [49] C.H. Kuo, Y. Tang, L.Y. Chou, B.T. Sneed, C.N. Brodsky, Z. Zhao, C.K. Tsung, Yolk-shell nanocrystal@ZIF-8 nanostructures for gas-phase heterogeneous catalysis with selectivity control, *J. Am. Chem. Soc.* 134 (2012) 14345–14348, <https://doi.org/10.1021/ja306869j>.
- [50] S. Wang, M. Zhang, W. Zhang, Yolk-shell catalyst of single Au nanoparticle encapsulated within hollow mesoporous silica microspheres, *ACS Catal.* 1 (2011) 207–211, <https://doi.org/10.1021/cs1000762>.
- [51] Z. Li, Z. Wang, B. Jiang, S. Kawi, Sintering resistant Ni nanoparticles exclusively confined within SiO₂ nanotubes for CH₄ dry reforming, *Catal. Sci. Technol.* 8 (2018) 3363–3371, <https://doi.org/10.1039/c8cy00767e>.
- [52] Z. Li, K. Sibudjing, Facile synthesis of multi-Ni-core@Ni phyllosilicate@CeO₂ shell hollow spheres with high oxygen vacancy concentration for dry reforming of CH₄, *ChemCatChem.* 10 (2018) 2994–3001, <https://doi.org/10.1002/cctc.201800335>.
- [53] Z. Li, L. Mo, Y. Kathiraser, S. Kawi, Yolk – satellite – shell structured Ni – Yolk@Ni@SiO₂ nanocomposite: superb catalyst toward methane CO₂ reforming reaction, *ACS Catal.* 4 (2014) 1526–1536, <https://doi.org/10.1021/cs401027p>.
- [54] L. Li, Y. Yao, B. Sun, Z. Fei, H. Xia, J. Zhao, W. Ji, C.-T. Au, Highly active and stable lanthanum-doped core-shell-structured Ni@SiO₂ catalysts for the partial oxidation of methane to syngas, *ChemCatChem.* 5 (2013) 3781–3787, <https://doi.org/10.1002/cctc.201300537>.
- [55] A.J. Majewski, J. Wood, Tri-reforming of methane over Ni@SiO₂ catalyst, *Int. J. Hydrogen Energy* 39 (2014) 12578–12585, <https://doi.org/10.1016/j.ijhydene.2014.06.071>.
- [56] H. Jiang, H. Li, H. Xu, Y. Zhang, Preparation of Ni/Mg_xTi_{1-x}O catalysts and investigation on their stability in tri-reforming of methane, *Fuel Process. Technol.* 88 (2007) 988–995, <https://doi.org/10.1016/j.fuproc.2007.05.007>.
- [57] K. a Dahlberg, J.W. Schwank, Synthesis of Ni@SiO₂ nanotube particles in a water-in-oil microemulsion template, *Chem. Mater.* 24 (2012) 2635–2644.
- [58] S. Das, J. Ashok, Z. Bian, N. Dewangan, M.H. Wai, Y. Du, A. Borgna, K. Hidajat, S. Kawi, Silica–ceria sandwiched Ni core–shell catalyst for low temperature dry reforming of biogas: Coke resistance and mechanistic insights, *Appl. Catal. B-Environ.* 230 (2018) 220–236, <https://doi.org/10.1016/j.apcatb.2018.02.041>.
- [59] J. Zhu, X. Peng, L. Yao, X. Deng, H. Dong, D. Tong, C. Hu, Synthesis gas production from CO₂ reforming of methane over Ni–Ce/SiO₂ catalyst: The effect of calcination ambience, *Int. J. Hydrogen Energy* 38 (2013) 117–126, <https://doi.org/10.1016/j.ijhydene.2012.07.136>.
- [60] T. Yang, R. Zhou, D.-W. Wang, S.P. Jiang, Y. Yamauchi, S.Z. Qiao, M.J. Monteiro, J. Liu, Hierarchical mesoporous yolk-shell structured carbonaceous nanospheres for high performance electrochemical capacitive energy storage, *Chem. Commun. (Camb.)* 51 (2015) 2518–2521, <https://doi.org/10.1039/C4CC09366F>.
- [61] J. Ashok, S. Kawi, Steam reforming of toluene as a biomass tar model compound over CeO₂ promoted Ni/CaO-Al₂O₃ catalytic systems, *Int. J. Hydrogen Energy* 38 (2013) 13938–13949, <https://doi.org/10.1016/j.ijhydene.2013.08.029>.
- [62] L. Zhang, M. Li, T. Ren, X. Liu, Ce-modified Ni nanoparticles encapsulated in SiO₂ for CO_x-free hydrogen production via ammonia decomposition, *Int. J. Hydrogen Energy* 40 (2015) 2648–2656, <https://doi.org/10.1016/j.ijhydene.2014.12.079>.
- [63] X. Du, D. Zhang, L. Shi, R. Gao, J. Zhang, Morphology dependence of catalytic properties of Ni/CeO₂ nanostructures for carbon dioxide reforming of methane, *J. Phys. Chem. C.* 116 (2012) 10009–10016, <https://doi.org/10.1021/jp300543r>.
- [64] P. Lakshmanan, M.S. Kim, E.D. Park, A highly loaded Ni@SiO₂ core-shell catalyst for CO methanation, *Appl. Catal. A-Gen.* 513 (2016) 98–105, <https://doi.org/10.1016/j.apcata.2015.12.038>.
- [65] K.M. Kang, H.W. Kim, I.W. Shim, H.Y. Kwak, Catalytic test of supported Ni catalysts with core/shell structure for dry reforming of methane, *Fuel Process. Technol.* 92 (2011) 1236–1243, <https://doi.org/10.1016/j.fuproc.2011.02.007>.
- [66] D. Iglesias, M. Melchionna, Enter the tubes: carbon nanotube endohedral catalysis, *Catalysts.* 9 (2019) 128, <https://doi.org/10.3390/catal9020128>.
- [67] L. Pino, A. Vita, M. Laganà, V. Recupero, Hydrogen from biogas: catalytic tri-reforming process with Ni/La-Ce-O mixed oxides, *Appl. Catal. B-Environ.* 148–149 (2014) 91–105, <https://doi.org/10.1016/j.apcatb.2013.10.043>.
- [68] B. Li, X. Xu, S. Zhang, Synthesis gas production in the combined CO₂ reforming with partial oxidation of methane over Ce-promoted Ni/SiO₂ catalysts, *Int. J. Hydrogen Energy* 38 (2013) 890–900, <https://doi.org/10.1016/j.ijhydene.2012.10.103>.
- [69] K.R. Krause, P. Schabes-Retchkiman, L.D. Schmidt, Microstructure of Rh-Ce particles on silica: interactions between Ce and SiO₂, *J. Catal.* 134 (1992) 204–219.
- [70] J.A. Farmer, C.T. Campbell, Ceria maintains smaller metal catalyst particles by strong metal-support bonding, *Science* 329 (2010) 933–936, <https://doi.org/10.1126/science.1191778>.
- [71] Y. Nagai, T. Hirabayashi, K. Dohmae, N. Takagi, T. Minami, H. Shinjoh, S. Matsumoto, Sintering inhibition mechanism of platinum supported on ceria-based oxide and Pt-oxide-support interaction, *J. Catal.* 242 (2006) 103–109, <https://doi.org/10.1016/j.jcat.2006.06.002>.
- [72] J.-H. Kim, D.J. Suh, T.-J. Park, K.-L. Kim, Effect of metal particle size on coking during CO₂ reforming of CH₄ over Ni-alumina aerogel catalysts, *Appl. Catal. A-Gen.* 197 (2000) 191–200, [https://doi.org/10.1016/S0926-860X\(99\)00487-1](https://doi.org/10.1016/S0926-860X(99)00487-1).
- [73] Z. Li, X. Hu, L. Zhang, S. Liu, G. Lu, Steam reforming of acetic acid over Ni/ZrO₂ catalysts: effects of nickel loading and particle size on product distribution and coke formation, *Appl. Catal. A-Gen.* 417–418 (2012) 281–289, <https://doi.org/10.1016/j.apcatb.2012.01.002>.
- [74] I. Luisetto, S. Tuti, C. Battocchio, S. Lo Mastro, A. Sodo, Ni/CeO₂-Al₂O₃ catalysts for the dry reforming of methane: the effect of CeAlO₃ content and nickel crystallite size on catalytic activity and coke resistance, *Appl. Catal. A-Gen.* 500 (2015) 12–22, <https://doi.org/10.1016/j.apcata.2015.05.004>.
- [75] J. Zhang, H. Wang, A.K. Dalai, Effects of metal content on activity and stability of Ni-Co bimetallic catalysts for CO₂ reforming of CH₄, *Appl. Catal. A-Gen.* 339 (2008) 121–129, <https://doi.org/10.1016/j.apcata.2008.01.027>.
- [76] K.O. Christensen, D. Chen, R. Lødeng, A. Holmen, Effect of supports and Ni crystal size on carbon formation and sintering during steam methane reforming, *Appl. Catal. A-Gen.* 314 (2006) 9–22, <https://doi.org/10.1016/j.apcata.2006.07.028>.
- [77] D. San-José-Alonso, J. Juan-Juan, M.J. Illán-Gómez, M.C. Román-Martínez, Ni, Co and bimetallic Ni–Co catalysts for the dry reforming of methane, *Appl. Catal. A-Gen.* 371 (2009) 54–59, <https://doi.org/10.1016/j.apcata.2009.09.026>.
- [78] I. Alstrup, A new model explaining carbon filament growth on nickel, iron, and Ni–Cu Alloy Catalysts, *J. Catal.* 109 (1988) 241–251.
- [79] R.K. Singh, A. Shukla, A. Yadav, L.N. Sivakumar Konathala, R. Bal, Effect of metal-support interaction on activity and stability of Ni-CeO₂ catalyst for partial oxidation of methane, *Appl. Catal. B-Environ.* 202 (2017) 473–488, <https://doi.org/10.1016/j.apcatb.2016.09.060>.
- [80] M. Khajenoori, M. Rezaei, F. Meshkani, Characterization of CeO₂ promoter of a nanocrystalline Ni/MgO catalyst in dry reforming of methane, *Chem. Eng. Technol.* 37 (2014) 957–963, <https://doi.org/10.1002/ceat.201300503>.
- [81] Z. Hou, J. Gao, J. Guo, D. Liang, H. Lou, X. Zheng, Deactivation of Ni catalysts during methane autothermal reforming with CO₂ and O₂ in a fluidized-bed reactor, *J. Catal.* 250 (2007) 331–341, <https://doi.org/10.1016/j.jcat.2007.06.023>.
- [82] Y. Lu, J. Xue, C. Yu, Y. Liu, S. Shen, Mechanistic investigations on the partial oxidation of methane to synthesis gas over a nickel-on-alumina catalyst, *Appl. Catal. A-Gen.* 174 (1998) 121–128, [https://doi.org/10.1016/S0926-860X\(98\)00163-X](https://doi.org/10.1016/S0926-860X(98)00163-X).
- [83] B.C. Enger, R.L. Lødeng, A. Holmen, Modified cobalt catalysts in the partial oxidation of methane at moderate temperatures, *J. Catal.* 262 (2009) 188–198, <https://doi.org/10.1016/j.jcat.2008.12.014>.